RSC Applied Interfaces

ROYAL SOCIETY OF CHEMISTRY

PAPER

View Article Online
View Journal | View Issue

Check for updates

Cite this: *RSC Appl. Interfaces*, 2024, **1**, 920

High-performance functionalized anthracene organic supercapacitors†

Sudipta Biswas, [a] Rajendran Manikandan, [a] Nitzan Shauloff, [a] Shubhra Kanti Bhaumik [a] and Raz Jelinek *[ab]

Received 3rd March 2024,
Accepted 5th April 2024

DOI: 10.1039/d4lf00076e

rsc.li/RSCApplInter

Organic supercapacitors have attracted significant interest as promising energy storage vehicles due to their favorable electrochemical properties, synthetic versatility, low cost, and environmental friendliness. We constructed supercapacitor electrodes comprising anthracene derivatives as the core component. Specifically, anthracene linked to functionalized ethylene displaying different electron acceptors endows the electrodes with tunable energy gaps and concomitant redox potentials. The conjugated anthracene units in such systems furnished the structural framework *via* adopting a crystalline nanorod organization *via* π–π stacking, while the delocalized electrons likely participated in the reversible redox reactions contributing to electrode pseudocapacitance. Asymmetric supercapacitors consisting of *tert*-butyl-ethylene-ketone-anthracene/polyaniline as the cathode were constructed, featuring excellent electrochemical performance. Specifically, the asymmetric device using an ionic liquid electrolyte displayed a broad voltage window, high cycling stability, and an energy density of 30 W h kg^{-1} at a power density of 620 W kg^{-1}. Overall, we show that anthracene derivatives provide powerful redox-tunable electrode building blocks, expanding the molecular toolbox for organic supercapacitors.

Introduction

Supercapacitors are important components in charge storage technologies due to their high-power density, moderately high energy density, fast charge–discharge, and cycling capabilities. The majority of conventional supercapacitors comprise transition metal-based oxides or other inorganic materials, which exhibit limitations due to high weight, environmental hazards, and high manufacturing costs. Organic supercapacitors have attracted interest as viable alternatives due to their less adverse environmental impact, structural and functional variability, and pseudocapacitive properties enhancing their charge storage capacities.

Accounting for considerable scientific and technological interest, new organic electrode materials (OEMs) are sought.[1] Conducting polymers such as polyaniline (PANI), polypyrrole (Ppy), and polythiophene (PTh) have been used as core electrode components in organic supercapacitors.[2,3] Other organic electrodes are composed of heteroatom-doped carbon materials,[4,5] covalent organic framework (COF) assemblies,[6,7] and others.[8,9] Yet, major impediments for wider implementation of organic supercapacitors include identification of high-performance chemical species employed in electrode construction, technical challenges in device fabrication, low stability, and insufficient cycling properties.

Quinone-based compounds, particularly conjugated cyclic diketones, have been used in organic supercapacitors accounting for their high energy density, low cost, structural stability, redox activity, and environmental stability.[10,11] Poly(1,5-diaminoanthraquinone), for example, has been employed in efficient supercapacitor electrodes.[12] However, major drawbacks of this quinone include low intrinsic conductivity and rapid self-discharge.[13] Despite these challenges, quinones present untapped potential in energy storage applications as they display tunable functional groups allowing modulation of redox properties.

Anthracene is a rigid polycyclic conjugated aromatic hydrocarbon, exhibiting high fluorescence and light absorbance. Anthracene derivatives have been widely used in organic light-emitting diodes,[14] as fluorescence probes,[15] electrochromic materials,[16] and dye-sensitized solar cells.[17] Functionalized anthracenes have been utilized as battery components;[18] however, anthracene has not been employed in supercapacitor devices due to its high energy gap. Anthraquinones have been employed as constituents of

[a] *Department of Chemistry, Ben Gurion University of the Negev, Beer Sheva 8410501, Israel. E-mail: razj@bgu.ac.il*
[b] *Ilse Katz Institute for Nanotechnology, Ben Gurion University of the Negev, Beer Sheva 8410501, Israel*

† Electronic supplementary information (ESI) available. See DOI: https://doi.org/10.1039/d4lf00076e

supercapacitor electrodes, accounting for their high structural diversity due to their abundance, tunability with functional groups, superior electrochemical stability, high active material utilization and facile redox kinetics.[19,20]

Here, we demonstrate the use of functionalized anthracenes as key components of organic supercapacitor electrodes. Specifically, we synthesized anthracenes with residues exhibiting different electron accepting/donating properties and investigated the electrochemical properties of the molecules. We particularly demonstrate that the anthracene backbone aids the assembly of stable high surface area structures, and further accommodates different functional groups allowing modulation of redox properties. Electrodes comprising *tert*-butyl-ethylene-ketone-anthracene and polyaniline, used as conductivity- and capacitance-enhancing additives, were fabricated and employed as cathodes in high-performance asymmetric supercapacitors. Importantly, we show that *tert*-butyl-ethylene-ketone-anthracene displayed a significant contribution to the electrode pseudocapacitance. Asymmetric supercapacitors utilizing an ionic liquid electrolyte featured excellent electrochemical properties, specifically a wide device voltage window, high energy density, and cycling stability. Overall, the anthracene derivatives constitute useful building blocks for organic supercapacitor design and may be readily employed in practical charge storage devices.

Results and discussion

Physicochemical properties of the anthracene derivatives

Scheme 1 depicts the chemical structures of the anthracene-based derivatives 2-(anthracen-9-ylmethylene)-malononitrile (denoted **cyano-ethylene-ANT**),[21] (*E*)-4-(anthracen-9-yl)-but-3-en-2-one (**methyl-ethylene-ketone-ANT**),[22] and (*E*)-1-(anthracen-9-yl)-4,4-dimethylpent-1-en-3-one (***tert*-butyl-ethylene-ketone-ANT**).[23] The anthracene-attached units in the derivatives furnish different electron migration properties, as the two cyano units and the ketones are strong electron acceptors, whereas the methyl and particularly *tert*-butyl residues in methyl-ethylene-ketone-ANT and *tert*-butyl-ethylene-ketone-ANT are electron donors.[24]

The electrochemical properties of the anthracene derivatives were studied (Fig. 1). Cyclic voltammetry (CV) analysis in Fig. 1A illustrates the redox profiles of the anthracene derivatives and concomitant energy levels calculated from the CV curves. The CV curves in Fig. 1A were recorded at a 50 mV s^{-1} scan rate

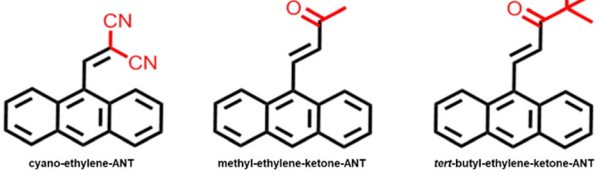

Scheme 1 Chemical structures of the anthracene (ANT) derivatives.

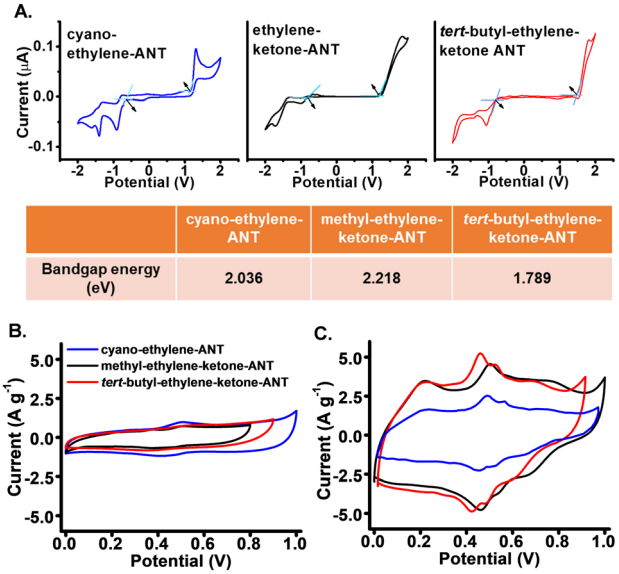

	cyano-ethylene-ANT	methyl-ethylene-ketone-ANT	*tert*-butyl-ethylene-ketone-ANT
Bandgap energy (eV)	2.036	2.218	1.789

Fig. 1 Electrochemical properties of the anthracene derivatives. A. CV curves of the materials using an organic electrolyte and a glassy carbon electrode with a wide potential range and tabulated HOMO–LUMO energy gaps calculated from the corresponding CV curves. B. CV curves of the anthracene derivatives deposited on graphite electrodes. C. CV curves of drop-cast films of the anthracene derivatives mixed with PANI (3 : 7 weight ratio).

using a three-electrode system consisting of glassy carbon as the working electrode, platinum wire as the counter electrode, and Ag/Ag^+ as the reference electrode. The onset oxidation potentials (E_{ox}) and reduction potentials (E_{red}) were determined from the baseline intercepts of the tangents applied at the inflection points in the CV curves, which yielded the HOMO–LUMO bandgap energies (E_g) using the ferrocene redox (FOC/FOC^+) system as a reference, according to the following equations:[25]

$$E_{HOMO} = -(E_{(ox)onset} + 4.8 - E_{FOC})$$

$$E_{LOMO} = -(E_{(red)onset} + 4.8 - E_{FOC})$$

$$E_g = -(E_{HOMO} - E_{LOMO})$$

in which 4.8 eV is the reference energy of the ferrocene energy level and E_{FOC} is the potential of FOC/FOC^+ *versus* Ag/AgCl (0.54 eV, as measured by cyclic voltammetry). The table in Fig. 1A depicts the calculated bandgap energies, which are in a lower range as reported for organic semiconductors,[26,27] pointing to the possible utilization of the anthracene derivatives in supercapacitor devices.

We further tested the anthracene derivatives as working electrodes in electrochemical devices (Fig. 1B and C). Fig. 1B depicts the CV curves of drop-cast thin films of the anthracene derivatives on the graphite sheet, employed as the current collector. As apparent in Fig. 1B, the specific

capacitance of the cyano-ethylene-ANT electrode (reflected in the area enclosed in the CV curve) is the most pronounced (~180 F g^{-1}), accounting for the lowest bandgap energy of this derivative (*i.e.*, Fig. 1A). The peaks in Fig. 1B likely correspond to the redox reactions associated with the –CN and ═O functional groups, *i.e.*, CN ↔ CN^- and O + H^+(aq) + e^- ↔ OH.[28,29]

To increase the electrode capacitance for usage in supercapacitor device design, we fabricated mixed electrodes comprising interspersed anthracene derivatives and polyaniline (PANI), a conductive polymer widely employed to enhance conductivity and electrochemical properties in supercapacitor electrodes (Fig. 1C).[30,31] Indeed, the specific capacitance values calculated for the composite electrodes from the CV curves in Fig. 1C (recorded at 5 mV s^{-1}) were significantly higher than those for the electrodes comprising only the derivatives (*i.e.*, Fig. 1B). Interestingly, Fig. 1C reveals that in contrast to the pure compound electrodes, *tert*-butyl-ethylene-ketone-ANT/PANI and methyl-ethylene-ketone-ANT/PANI exhibited a higher specific capacitance than cyano-ANT/PANI. This result may be due to more pronounced interactions and concomitant dispersion of *tert*-butyl-ethylene-ketone-ANT or methyl-ethylene-ketone-ANT with PANI *via* hydrogen bonding between the amine moieties of PANI and ketone groups within the ANT molecules.[32,33] The shapes of the CV curves of *tert*-butyl-ethylene-ketone-ANT/PANI and methyl-ethylene-ketone-ANT/PANI indicate contributions of both the pseudocapacitance and EDLC, as the pronounced redox peaks at around 0.5 V appear superimposed on the rectangular-shaped curves (Fig. 1C).

Based on the capacitance profile in Fig. 1C, we prepared electrodes comprising PANI and *tert*-butyl-ethylene-ketone-ANT and studied their electrochemical properties (Fig. 2). Fig. 2A, i depicts the CV curves recorded at a scan rate of 5 mV s^{-1} for a graphitic electrode coated with *tert*-butyl-ethylene-ketone-ANT/PANI composites at different weight ratios between the two constituents. The calculated specific capacitance values with respect to the percentage of PANI are also shown (Fig. 2A, ii). Fig. 2A indicates that the highest specific capacitance was obtained in a PANI weight concentration of 70%. The representative scanning electron microscopy (SEM) image of the *tert*-butyl-ethylene-ketone-ANT/PANI composite film at 70% PANI concentration in Fig. 2B reveals interspersed thin crystalline *tert*-butyl-ethylene-ketone-ANT aggregates within the PANI domains, underscoring a pronounced surface area, which accounts for the high capacitance apparent in this PANI concentration.[34] Indeed, *tert*-butyl-ethylene-ketone-ANT/PANI films at different weight ratios exhibited larger and less dispersed *tert*-butyl-ethylene-ketone-ANT aggregates (Fig. S1†). Brunauer, Emmett and Teller (BET) analysis in Fig. S2† confirms the enhanced surface area in the *tert*-butyl-ethylene-ketone-ANT/PANI (3 : 7 weight ratio) film.

Fig. 2C shows the powder XRD patterns of *tert*-butyl-ethylene-ketone-ANT, the *tert*-butyl-ethylene-ketone-ANT/PANI composite (3 : 7 weight ratio) and pristine PANI. While the XRD

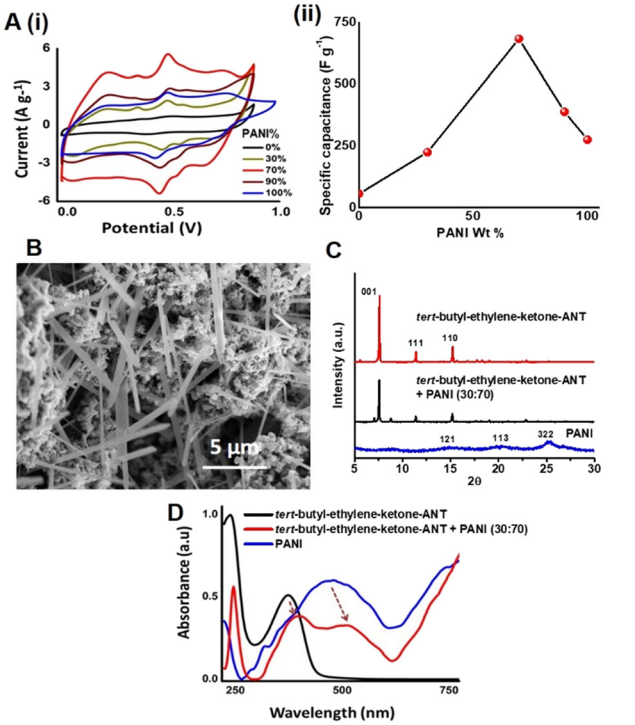

Fig. 2 Physicochemical properties of *tert*-butyl-ethylene-ketone-ANT/polyaniline electrodes. A. (i) CV curves of *tert*-butyl-ethylene-ketone-ANT/PANI at different weight percentages of PANI; (ii) the graph depicting the calculated specific capacitance *vs.* percentage of PANI. B. SEM micrograph of *tert*-butyl-ethylene-ketone-ANT/PANI (30 : 70 wt%). C. PXRD patterns of the drop-cast films. D. UV–vis absorbance spectra of the films.

pattern of PANI alone indicates a semi-crystalline organization, the appearance of sharp XRD peaks of *tert*-butyl-ethylene-ketone-ANT reflects a monoclinic crystalline structure, and echoes the SEM results (*i.e.*, Fig. 2B). The UV–vis spectra of the drop-cast films in Fig. 2D shed light on the interactions between *tert*-butyl-ethylene-ketone-ANT and PANI in the composite electrode. Specifically, Fig. 2D shows significant redshifts of both the *tert*-butyl-ethylene-ketone-ANT peak (from 385 nm in an electrode deposited with the pure molecule to 405 nm in the composite electrode) and the PANI signal (from 480 nm to 505 nm). This result likely accounts for the interactions between PANI and *tert*-butyl-ethylene-ketone-ANT, which contribute to the enhanced electrochemical properties.

Asymmetric supercapacitors using *tert*-butyl-ethylene-ketone-ANT/PANI electrodes

We fabricated a supercapacitor in which the *tert*-butyl-ethylene-ketone-ANT/PANI (3 : 7 weight ratio) electrode served as the cathode and reduced graphene oxide (rGO)/activated charcoal (AC) (1 : 1) was the anode. Both electrodes were prepared using small amounts of polymer binder (Nafion at 5 wt%) and coated on the graphite current collector (electrode properties are summarized in Fig. 3 and S3†). Fig. 3A presents the CV curves recorded at different scan rates within

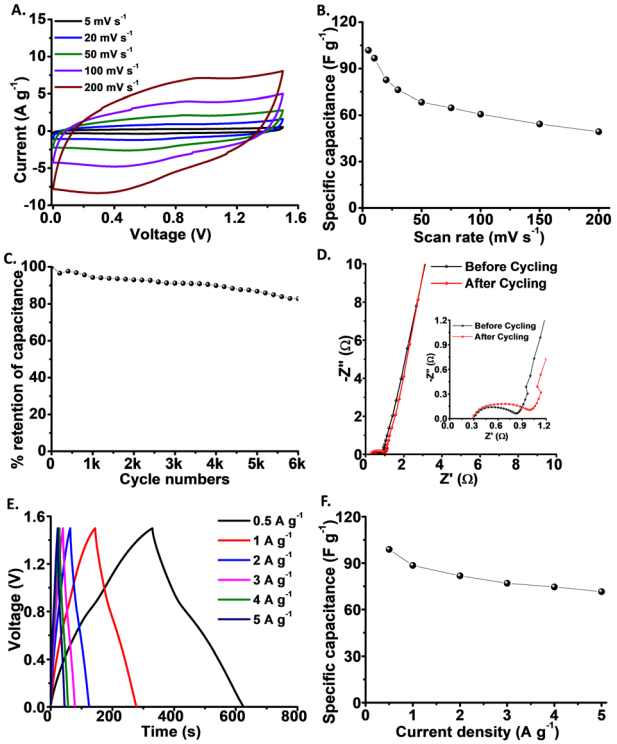

Fig. 3 Electrochemical properties of the *tert*-butyl-ethylene-ANT/PANI–reduced graphene oxide asymmetric supercapacitor, using an aqueous electrolyte. A. CV curves recorded at different scan rates. B. Specific capacitance calculated from the CV curves. C. Capacitance retention after different cycle numbers. D. Nyquist plot in a frequency range of 10 mHz–100 kHz (inset: Nyquist plot in the high-frequency range). Plots shown were recorded before (black) and after 6000 cycles (red). E. Galvanostatic charge–discharge (GCD) curves. F. Specific capacitance with respect to current density, calculated from the GCD curves.

a 1 V window using a 1 M H_2SO_4 aqueous electrolyte. The deviation from the rectangular appearance of the CV curves reflects a contribution from the redox reaction properties in *tert*-butyl-ethylene-ketone-ANT/PANI.[30,35]

The relationship between the capacitance and scan rate of the device is depicted in Fig. 3B. The calculated specific capacitance was 100 F g^{-1} at 5 mV s^{-1} with around 50% retention at a scan rate of 200 mV s^{-1}, which is high compared to similar organic supercapacitors, underscoring operation feasibility at high currents.[9,36–38] The stability of the device was further tested, indicating an excellent ~85% capacitance retention after 6000 cycles (Fig. 3C). We also carried out a cycling stability test for the system by recording initially 3000 cycles and additional 1000 cycles after a 72 hour pause, demonstrating a negligible (1%) drop in the specific capacitance (Fig. S4†).

Electrochemical impedance spectroscopy (EIS) measurements at a frequency range of 10 mHz–100 kHz were also carried out to evaluate the equivalent series resistance (R_s) and charge transfer resistance (R_{ct}) of the device (Fig. 3D). Following fitting to an equivalent circuit (the scheme of the circuit is presented in Fig. S5†), the calculated R_s was minimally reduced, from 0.30 Ω to 0.26 Ω, following the cycling experiments, while the R_{ct} increased from 0.49 Ω to 0.70 Ω, echoing the cycling stability analysis in Fig. 3C. These resistance values are on par or lower than those of the reported anthraquinone-based organic supercapacitors.[39–41]

Fig. 3E depicts the galvanostatic charge–discharge (GCD) curves recorded at different current densities, further reflecting the significant contribution of pseudocapacitance to energy storage by the supercapacitor. While the linear regions of the GCD curves are attributed to the EDLC mechanism, the shoulders correspond to the redox reactions undergone by the anthracene derivative.[8,30,42] Fig. 3F presents the specific capacitance calculated from the GCD curves, displaying a maximal specific capacitance of approximately 100 F g^{-1} at 1 A g^{-1}. Notably, 75% capacitance retention is observed at 5 A g^{-1} attesting to the operation of the device at high power.

We assembled an asymmetric supercapacitor using a non-aqueous, ionic liquid electrolyte, 1-ethyl-3-methylimidazolium hydrogen sulfate ($EMIM^+HSO_4^-$; concentration 1 M) in acetonitrile (Fig. 4). Fig. 4A presents the CV curves recorded

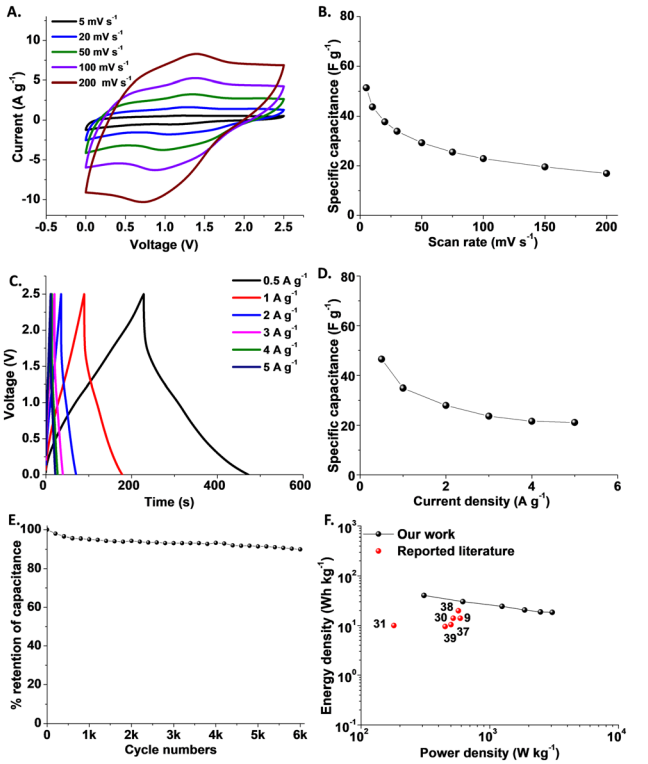

Fig. 4 Electrochemical properties of the *tert*-butyl-ethylene-ketone-ANT/PANI–rGO/AC asymmetric supercapacitor, using an ionic liquid electrolyte. A. CV curves recorded at different scan rates. B. Specific capacitance calculated from the CV curves. C. GCD curves recorded at different current densities. D. Specific capacitance with respect to current densities, calculated from the GCD curves. E. Cycling stability of the device. F. Ragone plot depicting the energy density as a function of power density. The black data points correspond to the device in this work, while the red points show previously published similar studies.[9,36,37,49–51]

at different scan rates in a voltage window of 2.5 V. Importantly, no disintegration of the electrolyte was observed even at a working voltage of 2.5 V, indicating a broad voltage window made possible by the ionic liquid electrolyte. Redox reactions, contributing to the small humps in the CV curves in Fig. 4A, are also observed. Fig. 4B presents the specific capacitance calculated at different scan rates obtained from the CV curves. The maximal specific capacitance of 50 F g^{-1} is high compared to other organic supercapacitors utilizing ionic liquid electrolytes.[43–45]

Fig. 4C depicts the GCD curves recorded in the range of 0.5–5 A g^{-1} within the 2.5 V potential window. The GCD curves are linear to a high extent, accounting for the dominant EDLC mechanism. The higher discharge times further reflect a significant specific capacitance. Notably, the GCD curve recorded at 0.5 A g^{-1} indicates a charging time of 240 s and a discharge time of 230 s (Fig. 4C), yielding a coulombic efficiency of 96%, which is significantly better than the values reported in many publications. Yet, using a different methodology based on calculating the area under the 1 A g^{-1} curve results in a coulombic efficiency of 71%, which is comparable to the values reported in many studies.[46–48]

Fig. 4D presents the relationship between the specific capacitance and current densities, obtained from the GCD curves in Fig. 4C, indicating a specific capacitance of 35 F g^{-1} at 1 A g^{-1} while a 60% capacitance retention was observed at 5 A g^{-1}, underscoring a good rate capability. The cycling experiments in Fig. 4E further attest to a high 92% capacitance retention after 6000 cycles. Self-discharge analysis (Fig. S13†) similarly indicates the excellent stability of the asymmetric device. The Ragone plot in Fig. 4F highlights the high energy and power densities of the *tert*-butyl-ethylene-ketone-ANT/PANI–rGO/AC asymmetric supercapacitor. Specifically, the device generated a high energy density of 30 W h kg^{-1} at a power of 620 W kg^{-1}, which is superior compared to many reported organic supercapacitor systems.[9,36–38,49–51]

Fig. 5 presents the application of the asymmetric *tert*-butyl-ethylene-ketone-ANT/PANI–rGO/AC supercapacitor with the ionic liquid as the electrolyte for powering a blue light-emitting diode (LED), taking advantage of the excellent energy and power densities (*e.g.*, Fig. 4F). Fig. 5A illustrates the packaging of two supercapacitor devices connected in series, thereby supplying a total voltage of 5 V. Following the charging of the series SCs, we observed light emission from the connected LED even three minutes after connection (Fig. 5B) to the supercapacitors stack, reflecting the high energy density of the device.

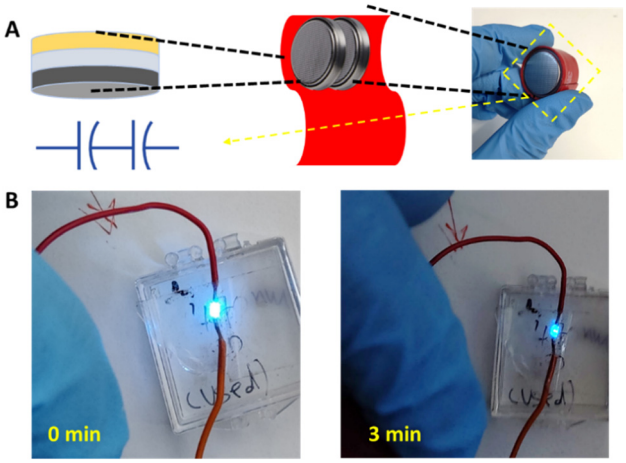

Fig. 5 Practical application of the *tert*-butyl-ethylene-ketone-ANT/PANI–AC asymmetric supercapacitor. A. Diagram showing two circular-shaped devices (packed in a CR2032 coin cell) connected in series. B. Photographs showing the usage of the device as an energy source to power a light-emitting diode (LED, 30 mA forward current), immediately (0 min) and 3 min after connecting to the device stack in series.

Conclusions

This study demonstrates a new supercapacitor design utilizing anthracene derivatives. We synthesized a functionalized anthracene molecule capable of showing redox activity – as a core electrode constituent in asymmetric supercapacitors, exhibiting excellent electrochemical properties. Specifically, an electrode comprising anthracene crystals interspersed with the conductive polymer polyaniline (PANI) featured high specific capacitance, good cycling stability, and low intrinsic resistance due to its high redox contribution from the combination of functional groups behaving as electron donors and acceptors. The *tert*-butyl-ethylene-ketone-ANT/PANI electrode generated a pronounced specific capacitance of 688 F g^{-1} at a 1 A g^{-1} current density. Asymmetric devices comprising anthracene and PANI as the cathode and AC as the anode yielded superior electrochemical properties. Overall, this work presents a new organic supercapacitor taking advantage of anthracene as a core compound having redox behaviour, which may be employed in practical charge storage devices.

Experimental section

Materials

Sodium hydroxide (NaOH), anthraldehyde, hydrochloric acid (HCl), malononitrile, ethyl acetate (EA), sodium sulphate (Na_2SO_4), and silica gel were purchased from Sigma Aldrich. Organic solvents including hexane, tetrachloromethane, toluene, dichloromethane, chloroform, acetone, dimethyl sulfoxide, ethyl acetate, and ethanol were purchased from Bio-Lab Ltd. (Jerusalem, Israel). 1-Ethyl-3-methylimidazolium hydrogen sulfate ionic liquid was purchased from Thermo Scientific-Alfa Aesar. The chemicals were used without further purification.

Synthesis of anthracene derivatives methyl-ethylene-ketone-ANT and *tert*-butyl-ethylene-ketone-ANT

Scheme 2 illustrates the synthesis route. A solution of ketone (5 ml) and 10% sodium hydroxide (5 ml) was placed in a round-bottom flask and the substituted anthraldehyde **1** (3 mmol) was added to the solution. Then, the reaction mixture was stirred at room temperature for 10 hours. After that, aq.

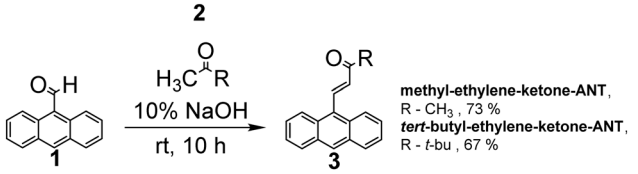

Scheme 2 Chemical synthesis of methyl-ethylene-ketone-ANT and *tert*-butyl-ethylene-ketone-ANT.

HCl solution was added to quench the reaction and the aqueous layer was extracted with EA (50 ml × 3). The combined organic layers were washed with brine (50 ml × 3), dried over anhydrous Na_2SO_4 and concentrated. The solvent was removed under reduced pressure, and the residue was chromatographed on silica gel (PE/EA) to obtain the desired product. All the products were confirmed by comparing their ^{1}H NMR data (shown in Fig. S7 and S8†) with those reported in previous reports.[52]

Synthesis of anthracene derivative cyano-ethylene-ANT

Scheme 3 depicts the synthesis route of cyano-ethylene-ANT. A solution of anthraldehyde **1** (3 mmol) and 10% sodium hydroxide (5 ml) in ethanol was added to malononitrile (5 mmol), and then the reaction mixture was stirred at room temperature for 9 hours. After that, aq. HCl solution was added to quench the reaction, and the aqueous layer was extracted with EA (50 mL × 3). The combined organic layers were washed with brine (50 mL × 3), dried over anhydrous Na_2SO_4 and concentrated. The solvent was removed under reduced pressure, and the residue was chromatographed on silica gel (PE/EA) to obtain the desired product. All the products were confirmed by comparing their ^{1}H NMR data (shown in Fig. S9†) with those reported in the previous literature.[52]

Characterization

Ultraviolet–visible (UV–vis) spectra were recorded on an Evolution 220 UV–visible spectrometer (Thermo Scientific, Madison, WI). Powder XRD measurements were carried out using a PANalytical Empyrean multi-purpose diffractometer. Scanning electron microscopy (SEM) images were recorded on a JEOL JSM-7400F scanning electron microscope (JEOL Ltd, Tokyo, Japan) and operated and analysed using the instrument software. Electrochemical measurements were performed in a three-electrode configuration, in which a graphite sheet current collector coated with the sample acted as the working electrode, platinum wire as the counter electrode, and Ag/AgCl as the reference electrode. 1 M H_2SO_4 was used as the electrolyte and the measurements were performed at different scan rates and current densities. The electrochemical measurements of the asymmetric supercapacitor device were performed in a two-electrode configuration. For electrochemical impedance spectroscopy measurement, a 5 mV AC signal in a frequency range of 1 MHz to 50 mHz was used. All the experiments were performed on a BioLogic SP-150 instrument (Seyssinet-Pariset, France).

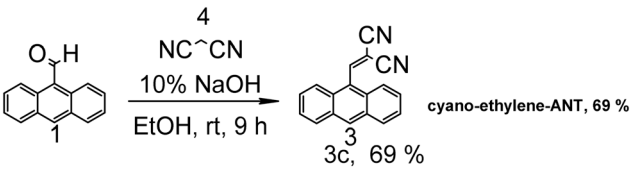

Scheme 3 Chemical synthesis of cyano-ethylene-ANT.

Preparation of the electrodes and asymmetric supercapacitors

10 mg of the anthracene derivatives were dissolved in 2 ml of ethanol and were vigorously mixed with perfluorinated resin solution containing Nafion in a material : Nafion weight ratio of 95 : 5 in ethanol, and drop-cast onto a graphite sheet (Farnell), which served as the current collector. Electrodes were kept at 70 °C for 2 h to dry. Similar electrodes were prepared using different concentrations of PANI and anthracene derivatives. Reduced graphene oxide and activated charcoal (50 : 50 wt%) were used as the anode, prepared by following the protocol as follows. 50 mg of the material was mixed with 5 wt% of Nafion solution in ethanol and dispersed well. Then, this mixture was drop-cast on a graphite current collector. Measurements were performed using 1 M aqueous H_2SO_4 solution as the electrolyte. When the electrodes are optimised, to prepare the device, a Whatman grade GF/A fine retention glass microfiber filter with a particle retention of 1.6 μm and a thickness of 260 μm was used as the separator with a CR2032 coin cell. For the non-aqueous asymmetric device, 1-ethyl-3-methylimidazolium hydrogen sulfate ($EMIM^+HSO^{4-}$; concentration = 1 M) in acetonitrile was used. All the device components were then packed in a CR2032 button cell to make a device. The mass loading of the device was 3 mg considering the window and specific capacitance of the individual electrodes after balancing the charges on both electrodes. Considering the specific capacitance of the distinct electrodes at 5 mV s^{-1}, we balanced the mass/charge using the formula $\left(\frac{m_+}{m_-} = \frac{C_- V_-}{C_+ V_+}\right)$ where m, C, and V represent the mass loading of the electrode, the specific capacitance obtained and the working potential window of the electrode, respectively. This was done for both positive and negative electrodes, represented as '+' and '–'.

Electrochemical data analysis

The specific capacitance values (C) from the cyclic voltammetry (CV) curves of the electrodes in the three-electrode configurations were estimated from eqn (1):

$$C = \int \frac{I dV}{2mv\Delta V} \quad (1)$$

whereas the specific capacitance for the device is calculated from eqn (2):

$$C = \int \frac{I\mathrm{d}V}{mv\Delta V} \quad (2)$$

where 'I' is the current at a specific potential, 'ΔV' is the potential/voltage window, 'm' is the mass of the active electrode material, and 'v' is the scan rate at which CV is performed.

The specific capacitance values from the galvanostatic charge/discharge curves of the three electrodes, as well as the device, were calculated using eqn (3):

$$C = \frac{I\Delta t}{m\Delta V} \quad (3)$$

where $\left(\frac{I}{m}\right)$ is the specific charge–discharge current, 'ΔV' is the potential/voltage window excluding voltage drop and 'Δt' is the discharge time of the electrode/device.

The energy density (E) of the electrode was calculated using eqn (4):

$$E = \frac{1}{2}CV^2 \quad (4)$$

and the power density (P) was calculated using eqn (5):

$$P = \frac{E}{\Delta t} \quad (5)$$

where the previous notations are used.

Author contributions

Conceptualization: S. Biswas, R. Manikandan, and R. Jelinek; data curation: S. Biswas and R. Manikandan; formal analysis: S. Biswas, R. Manikandan, N. Shauloff, S. K. Bhaumik, and R. Jelinek; funding acquisition: R. Jelinek; methodology: S. Biswas, R. Manikandan, and R. Jelinek; supervision: R. Jelinek; visualization: S. Biswas and R. Manikandan; writing – original draft: S. Biswas and R. Manikandan; writing – review & editing: N. Shauloff, S. K. Bhaumik, and R. Jelinek.

Conflicts of interest

There are no conflicts to declare.

Acknowledgements

The authors acknowledge the help from Dr. Nitzan Maman with the SEM measurements. Research was partly supported by grant award 1096/23, the Ministry of Energy, Israel.

References

1 Z. Wu, Q. Liu and P. Yang, *et al.*, *Electrochem. Energy Rev.*, 2022, **5**, 26.
2 A. Eftekhari, L. Li and Y. Yang, *J. Power Sources*, 2017, **347**, 86–107.
3 Q. Yang, Z. Hou and T. Huang, *J. Appl. Polym. Sci.*, 2015, **132**(11), 41615.
4 W. Li, G. Wang, W. Sui, T. Xu, L. Dai and C. Si, *Ind. Crops Prod.*, 2023, **204**, 117276.
5 Q. Abbas, R. Raza, I. Shabbir and A. G. Olabi, *J. Sci.: Adv. Mater. Devices*, 2019, **4**, 341–352.
6 M. Wang, H. Guo, R. Xue, Q. Li, H. Liu, N. Wu, W. Yao and W. Yang, *ChemElectroChem*, 2019, **6**, 2984–2997.
7 S. Kandambeth, V. S. Kale, O. Shekhah, H. N. Alshareef and M. Eddaoudi, *Adv. Energy Mater.*, 2021, **12**, 2100177.
8 R. Shi, C. Han, H. Duan, L. Xu, D. Zhou, H. Li, J. Li, F. Kang, B. Li and G. Wang, *Adv. Energy Mater.*, 2018, **8**, 1802088.
9 F. Ma, X. Wang, Z. Hu, L. Hou, Y. Yang, Z. Li, Y. He and H. Zhu, *Energy Fuels*, 2020, **34**, 13079–13088.
10 S. Suematsu and K. Naoi, *J. Power Sources*, 2001, **97–98**, 816–818.
11 S. Biswas and A. Chowdhury, *ChemPhysChem*, 2023, **24**, e202200567.
12 K. Naoi, S. Suematsu and A. Manago, *J. Electrochem. Soc.*, 2000, **147**, 420–426.
13 C. Han, H. Li, R. Shi, T. Zhang, J. Tong, J. Li and B. Li, *J. Mater. Chem. A*, 2019, **7**, 23378–23415.
14 J. Huang, J.-H. Su and H. Tian, *J. Mater. Chem.*, 2012, **22**, 10977.
15 H. Lu, B. Xu, Y. Dong, F. Chen, Y. Li, Z. Li, J. He, H. Li and W. Tian, *Langmuir*, 2010, **26**, 6838–6844.
16 N. Guven and P. Camurlu, *Polymer*, 2015, **73**, 122–130.
17 K. R. Justin Thomas, P. Singh, A. Baheti, Y.-C. Hsu, K.-C. Ho and J. T. s. Lin, *Dyes Pigm.*, 2011, **91**, 33–43.
18 M. R. Gerhardt, L. Tong, R. Gómez-Bombarelli, Q. Chen, M. P. Marshak, C. J. Galvin, A. Aspuru-Guzik, R. G. Gordon and M. J. Aziz, *Adv. Energy Mater.*, 2016, **7**, 1601488.
19 N. Qi, B. Yao, H. Sun, Y. Gao, X. Liu and F. Li, *Arabian J. Chem.*, 2023, **16**, 105263.
20 M. Oshitani, H. Yufu, K. Takashima, S. Tsuji and Y. Matsumaru, *J. Electrochem. Soc.*, 2019, **136**, 1590–1593.
21 J.-I. Aihara, K. Araya, K. Chiba and Y. Matsunaga, *Adv. Mol. Relax. Interact. Processes*, 1980, **18**, 199–210.
22 A. Mustafa, *Science*, 1950, **112**, 440.
23 H. Pang and P. G. Williard, *Tetrahedron*, 2020, **76**, 130913.
24 P. Bisel, L. Al-Momani and M. Müller, *Org. Biomol. Chem.*, 2008, **6**, 2655.
25 R. Manikandan, N. Shauloff, A. Nandi, A. Pevzner, S. Marx and R. Jelinek, *J. Mater. Chem. C*, 2022, **10**, 5458–5465.
26 J. C. S. Costa, R. J. S. Taveira, C. F. R. A. C. Lima, A. Mendes and L. M. N. B. F. Santos, *Opt. Mater.*, 2016, **58**, 51–60.
27 P. I. Djurovich, E. I. Mayo, S. R. Forrest and M. E. Thompson, *Org. Electron.*, 2009, **10**, 515–520.
28 R. Wang, M. Shi, L. Li, Y. Zhao, L. Zhao and C. Yan, *Chem. Eng. J.*, 2023, **451**(2), 138652.
29 L. Yan, C. Zhao, Y. Sha, Z. Li, T. Liu, M. Ling, S. Zhou and C. Liang, *Nano Energy*, 2020, **73**, 104766.
30 S. Biswas, N. Shauloff, R. Bisht and R. Jelinek, *Adv. Sustainable Syst.*, 2023, **7**, 2300035.
31 A. Chowdhury, S. Biswas, D. Mandal and A. Chandra, *J. Alloys Compd.*, 2022, **902**, 163733.
32 E. S. Matveeva, I. Hernández-Fuentes, V. Parkhutik and R. Díaz-Calleja, *Synth. Met.*, 1996, **83**, 181–184.

33 M. C. Pham, S. Hubert, B. Piro, F. Maurel, H. Le Dao and H. Takenouti, *Synth. Met.*, 2004, **140**, 183–197.
34 M. Oehzelt, G. Heimel, R. Resel, P. Puschnig, K. Hummer, C. Ambrosch-Draxl, K. Takemura and A. Nakayama, *J. Chem. Phys.*, 2003, **119**, 1078–1084.
35 L. Eliad, G. Salitra, A. Soffer and D. Aurbach, *J. Phys. Chem. B*, 2001, **105**, 6880–6887.
36 F. Ma, Z. Hu, L. Jiao, X. Wang, Y. He, Y. Yang and Z. Li, *ACS Appl. Energy Mater.*, 2021, **4**, 5493–5503.
37 Z. Algharaibeh and P. G. Pickup, *Electrochem. Commun.*, 2011, **13**, 147–149.
38 H.-C. Jung, R. Vinodh, C. V. V. M. Gopi, M. Yi and H.-J. Kim, *Mater. Lett.*, 2019, **257**, 126732.
39 C. Chen, Y. Li, C. Qian, L. Han, Z. Lu and L. Liu, *J. Mater. Chem. C*, 2023, **11**, 7441–7450.
40 S. Ryu, E. Kim and J. Yoo, *Electrochim. Acta*, 2021, **370**, 137809.
41 G. Ma, F. Hua, K. Sun, E. Feng, Z. Zhang, H. Peng and Z. Lei, *Ionics*, 2017, **24**, 549–561.
42 S. Arunachalam, B. Kirubasankar, V. Murugadoss, D. Vellasamy and S. Angaiah, *New J. Chem.*, 2018, **42**, 2923–2932.
43 S. Yamazaki, T. Ito, M. Yamagata and M. Ishikawa, *Electrochim. Acta*, 2012, **86**, 294–297.
44 S. Sathyamoorthi, V. Suryanarayanan and D. Velayutham, *J. Power Sources*, 2015, **274**, 1135–1139.
45 Q. Fan, R. Zhao, M. Yi, P. Qi, C. Chai, H. Ying and J. Hao, *Chem. Eng. J.*, 2022, **428**, 131107.
46 M. C. Devendrachari, G. Shimoga, S.-H. Lee, Y. H. Heo, H. M. N. Kotresh, M. O. Thotiyl, S.-Y. Kim and D.-S. Choi, *J. Energy Storage*, 2022, **56**, 106033.
47 J. El Nady, A. Shokry, M. Khalil, S. Ebrahim, A. M. Elshaer and M. Anas, *Sci. Rep.*, 2022, **12**, 3611.
48 J. Yang, H. Li, S. He, H. Du, K. Liu, C. Zhang and S. Jiang, *Polymers*, 2022, **14**, 2521.
49 B. Luo, Y. Chen, Y. Zhang and J. Huo, *New J. Chem.*, 2021, **45**, 17278–17286.
50 L. Jiao, Z. Hu, F. Ma, Y. He, Q. Zhou, L. Xiao, L. Lv and Y. Yang, *J. Energy Storage*, 2022, **52**, 104777.
51 S. Li, X. Wang, L. Hou, X. Zhang, Y. Zhou, Y. Yang and Z. Hu, *Electrochim. Acta*, 2019, **317**, 437–448.
52 M. Cui, M. Ono, H. Kimura, B. Liu and H. Saji, *J. Med. Chem.*, 2011, **54**, 2225–2240.